High-Scalability CMOS Quantum Magnetometer With Spin-State Excitation and Detection of Diamond Color Centers

Mohamed I. Ibrahim, *Student Member, IEEE*, Christopher Foy, Dirk R. Englund, *Member, IEEE*, and Ruonan Han, *Senior Member, IEEE*

***Abstract*— Magnetometers based on quantum mechanical processes enable high sensitivity and long-term stability without the need for re-calibration, but their integration into fieldable devices remains challenging. This article presents a CMOS quantum vector-field magnetometer that miniaturizes the conventional quantum sensing platforms using nitrogen-vacancy (NV) centers in diamond. By integrating key components for spin control and readout, the chip performs magnetometry through optically detected magnetic resonance (ODMR) through a diamond slab attached to a custom CMOS chip. The ODMR control is highly uniform across the NV centers in the diamond, which is enabled by a CMOS-generated ∼2.87 GHz magnetic field with <5% inhomogeneity across a large-area current-driven wire array. The magnetometer chip is 1.5 mm^2 in size, prototyped in 65-nm bulk CMOS technology, and attached to a 300 × 80 μm^2 diamond slab. NV fluorescence is measured by CMOS-integrated photodetectors. This ON-chip measurement is enabled by efficient rejection of the green pump light from the red fluorescence through a CMOS-integrated spectral filter based on a combination of spectrally dependent plasmonic losses and diffractive filtering in the CMOS back-end-of-line (BEOL). This filter achieves a measured ∼25 dB of green light rejection. We measure a sensitivity of 245 nT/Hz$^{1/2}$, marking a 130× improvement over a previous CMOS-NV sensor prototype, largely thanks to the better spectral filtering and homogeneous microwave generation over larger area.**

***Index Terms*— CMOS, field homogeneity, magnetometry, nanophotonic filter, nitrogen-vacancy (NV) centers, quantum, Zeeman.**

Manuscript received March 30, 2020; revised July 16, 2020 and August 31, 2020; accepted September 19, 2020. Date of publication October 9, 2020; date of current version February 24, 2021. This article was approved by Associate Editor David Stoppa. This work was supported in part by the National Science Foundation (NSF) Research Advanced through the Interdisciplinary Science and Engineering (RAISE) Transformational Advances in Quantum Systems (TAQS) under Grant 1839159, in part by the MIT Center for Integrated Circuits and Systems, Singapore-MIT Research Alliance (Low Energy Electronic Systems IRG), in part by the Army Research Office MURI on "Imaging and Control of Biological Transduction using NV-Diamond," and in part by the Gordon & Betty Moore Foundation. This is the extended version of an article originally presented at the IEEE Solid-State Circuit Conference (ISSCC), San Francisco, CA, USA, February 2019. *(Mohamed I. Ibrahim and Christopher Foy contributed equally to this work.) (Corresponding author: Mohamed I. Ibrahim.)*

The authors are with the Department of Electrical Engineering and Computer Science, Massachusetts Institute of Technology, Cambridge, MA 02139 USA (e-mail: ibrahimm@mit.edu; cfoy3@mit.edu; englund@mit.edu; ruonan@mit.edu).

Color versions of one or more of the figures in this article are available online at https://ieeexplore.ieee.org.

Digital Object Identifier 10.1109/JSSC.2020.3027056

I. Introduction

SOLID-STATE quantum sensors are attracting broad interest thanks to a combination of excellent sensitivity and long-term stability. In particular, ensembles of nitrogen-vacancy (NV) centers in diamond have emerged as an outstanding *room-temperature* sensor platform [1]–[5]. Ensemble NV-based magnetometry has achieved sensitivities at or below the picotesla level [6], [7], with applications ranging from bacteria magnetic imaging [4], NMR spectroscopy [8] to wide-field microscopy of superconducting materials [9]. However, an impediment to fieldable devices lies in the co-integration of different subsystems needed for optically detected magnetic resonance (ODMR), including microwave generation/delivery to diamond, optical excitation, filtering, and fluorescence-based spin detection (see Section II).

We recently addressed this integration problem by performing ODMR with a custom-designed CMOS circuit coupled to a diamond NV ensemble [10], [11]. However, insufficient pump light rejection and limited area of homogeneous microwave driving fields for the ODMR measurements posed a major limitation on achievable magnetic field sensitivity. Here, we present a new CMOS prototype that addresses these problems to achieve >100× sensitivity improvement, down to 245 nT/Hz$^{1/2}$ [12].

This article is organized as follows. Section II summarizes the basics quantum magnetometry and reviews the first NV-CMOS prototype [10], [11]. Section III describes the improved chip architecture, which incorporates high-homogeneity microwave delivery in addition to optical filtering that is based on plasmonic and Talbot effects. The chip is realized in a 65-nm CMOS process. Section IV presents performance measurements. Section V concludes with an outlook on further improvements to magnetometry and the incorporation of additional quantum sensing functions.

II. Background and Prior Research

A negatively charged NV center in diamond consists of a nitrogen atom adjacent to a vacancy in the carbon lattice (see Fig. 1(a)). The hybridization of the two unpaired electrons leads to a quantum system with the energy-level diagram shown in Fig. 1(b). The spin magnetic triplet is formed at the ground state (^{3}A), consisting of a sub-level $|m_s = 0\rangle$

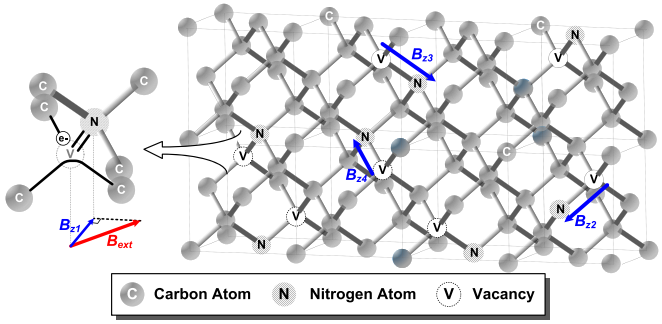

(a)

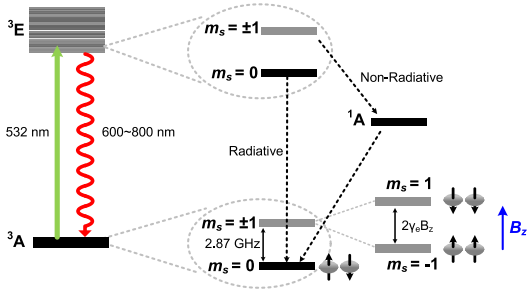

(b)

Fig. 1. (a) Negatively charged NV centers in a diamond lattice. The projections ($\vec{B}_{z1}$, $\vec{B}_{z2}$, $\vec{B}_{z3}$, $\vec{B}_{z4}$) of an external magnetic field $\vec{B}_{\text{ext}}$ along the four NV axes are also shown. (b) Energy-level diagram of a NV center.

at its lowest energy and another two zero-field degenerate sub-levels $|m_s = \pm 1\rangle$ raised by ~2.87 GHz. When an external magnetic field $\vec{B}_{\text{ext}}$ with a component $\vec{B}_z$ along the N-V axis (see Fig. 1(a)) is applied, the $|m_s = \pm 1\rangle$ sub-levels are split apart (i.e. Zeeman effect). The photon frequency Δf associated with such an energy gap is proportional to $|\vec{B}_z|$

$$\Delta f = f_+ - f_- = 2\gamma_e |\vec{B}_z| \tag{1}$$

where γ_e is the gyromagnetic ratio and equals 28 GHz/T, and f_+ and f_- are the frequencies for the transitions from $|m_s = 0\rangle$ to $|m_s = +1\rangle$ and $|m_s = -1\rangle$, respectively. We use Δf to derive $\vec{B}_z$.

NV magnetometry is performed by determining f_+ and f_- via ODMR [1]. In an ODMR experiment, the NV center spins are stimulated to their excitation states (^{3}E in Fig. 1(b)) with green light ($\lambda \approx 532$ nm), and then relax back to the ground state (^{3}A). The relaxation of the $|m_s = 0\rangle$ state is accompanied by bright red fluorescence ($\lambda \approx$ 600–800 nm). In contrast, when the $|m_s = \pm 1\rangle$ states are excited and relax back, they can undergo an intersystem crossing into a metastable spin-singlet state (^{1}A in Fig. 1(b)), and then into the $|m_s = 0\rangle$ ground level [11] reducing the red fluorescence intensity. Thus, static or slowly varying magnetic fields $\vec{B}_z$, can be determined by sweeping a microwave frequency f_{RF} around 2.87 GHz and monitoring the average intensity. The observed resonances of Fig. 2 are f_+ and f_-, which give $\vec{B}_z$.

NV centers have four known orientations (Fig. 1(a)) which separately lay along the tetrahedral axes of the host diamond. Accordingly, an external magnetic field $\vec{B}_{\text{ext}}$ has four projections – $\vec{B}_{z1}$, $\vec{B}_{z2}$, $\vec{B}_{z3}$, $\vec{B}_{z4}$ – along the NV orientations. This leads to four pairs of splitting in a single ODMR

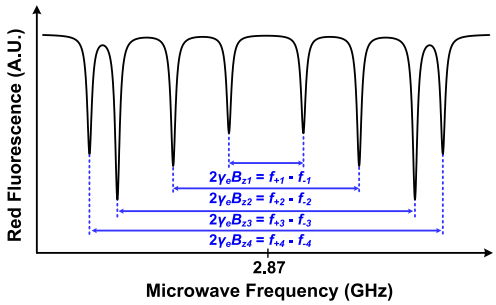

Fig. 2. Red-fluorescence intensity of the diamond at varying microwave frequency. An external magnetic-field bias with projections along the four N-V axes is assumed.

measurement (Fig. 2). The magnetometer based on this principle, therefore, has a vector-field measurement capability by monitoring the different magnetic field projects and reconstructing $\vec{B}_{\text{ext}}$. That is advantageous over conventional Hall and fluxgate-based sensors, where three devices in *x*-, *y*-, *z*-axes are needed for vector detection.

To explore the feasibility of a chip-scale, low-cost quantum magnetometer, a custom-designed CMOS prototype was realized and reported, for the first time, in [10]. This chip, using TSMC 65-nm CMOS technology, integrates most of the critical components (except the green light source) for the ODMR operation. Using this hybrid CMOS-NV-center integration platform, the ODMR spectrum of a nanodiamond layer attached on top of the chip is demonstrated. The estimated sensitivity of the system is 73 μT/Hz$^{1/2}$. Since the lattice orientations in the nanodiamond particles are random, the amount of frequency splitting in each NV is also random. As a result, this prototype cannot be used for vector-field sensing. Recently, we attached a film of bulk diamond (with uniform and well-defined lattice structure) to the same CMOS chip and demonstrated vector-sensing capability with 32 μT/Hz$^{1/2}$ sensitivity [11].

Our first CMOS prototype demonstrates the basic concept of chip-scale miniaturization of NV-center quantum sensors. The achieved sensitivity is still limited by two main factors: 1) in our experiments we observed that the dominant noise source was the shot noise due to the green light despite the presence of the grating filter [11]. Ideally, this sensor would be limited to the red fluorescence shot noise and therefore, a higher green-to-red suppression ratio is required for the integrated photonic filter. We estimated that, for the diamonds used in [10], [11], the intensity of red fluorescence is about 40–50 dB lower than that of the incident green light. Ultimately, an additional 30-dB out-of-band rejection is required for the photonic filter, so that the majority of photodiode noise is no longer generated by the green background and 2) the sensing area used is only 50 μm $\times$ 50 μm. This limits the number of NV centers, N. Increasing N improves the sensitivity due to larger red-fluorescence intensity (hence the *SNR* of the ODMR spectrum). This can be achieved by using a larger sensing area and higher NV-center density in diamond. Note that the *SNR* has the following dependence with N:

$$\text{SNR is} \begin{cases} \propto N & \text{when noise is green-light limited} \\ \propto \sqrt{N} & \text{when noise is red-light limited.} \end{cases} \tag{2}$$

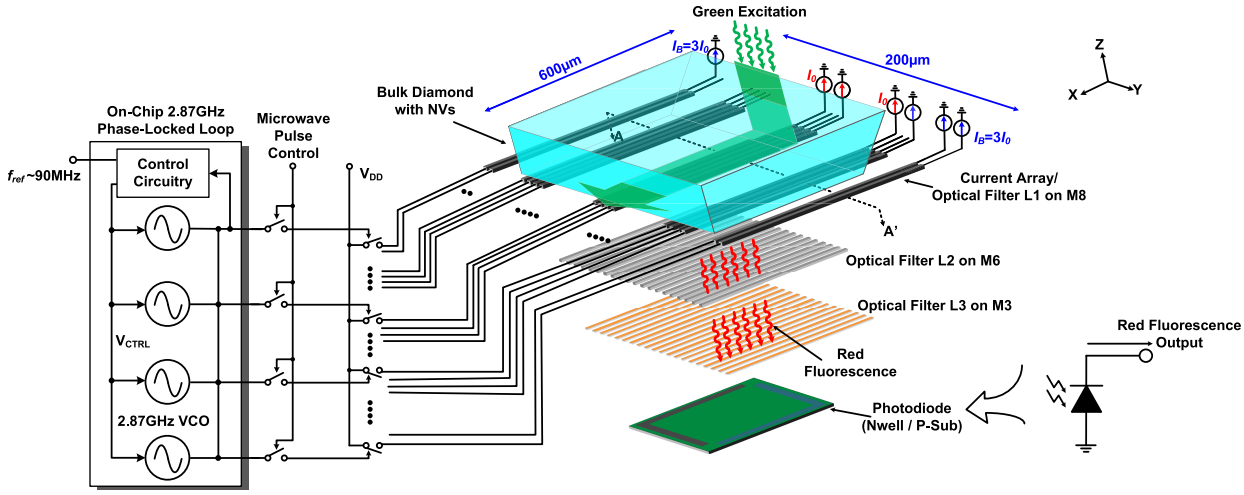

Fig. 3. Overall schematic of the CMOS quantum magnetometer with high scalability.

III. Scalable CMOS-NV Magnetometer for Enhanced Sensitivity

In this section, the design details of a new-generation CMOS-NV magnetometer [12] are provided. The highly scalable architecture of our CMOS-NV magnetometer allows for the microwave driving of NVs over a large area. The photodiode noise is further reduced with the adoption of a new ON-chip photonic filter. These structures are co-designed with the ON-chip electronics.

A. Systematic Architecture of the Chip

The overall schematic of the CMOS-NV magnetometer is given in Fig. 3. Shown on the left of Fig. 3 is an ON-chip phase-locked loop (PLL) which generates the 2.87-GHz microwave signal (see Section III-E). To drive the NVs with the ON-chip generated microwave field, an array of current-driven linear wires are implemented using the M8 of the chip, of which the driving currents are toggled by the PLL output. Such a design addresses a major challenge regarding the uniformity of the microwave magnetic field over a large area. In Section III-B, detailed explanations of the microwave launcher are provided. In this work, a diamond area of $\sim 500 \times 500\ \mu m^2$ is excited by the microwave. The sensing area with uniform microwave excitation is limited to $300 \times 80\ \mu m^2$ as discussed in Section III-D. Shown in Sections III-C and III-D, the current-driven wire array, along with additional two layers of metal gratings, also form a photonic filter in order to suppress the green light transmitted through the diamond placed on top of the chip. Finally, the spin-dependent red fluorescence of the NV centers is measured using an n-well/p-substrate photodiode.

B. Generation of High-Homogeneity Magnetic Field

Our NV-CMOS sensor interrogates an ensemble of NV centers to perform magnetometry. The microwave field strength determines both the ODMR resonance amplitude (contrast) and the resonance linewidth. Optimizing the sensitivity requires maximizing the contrast while minimizing the resonance linewidth [13]. For ensembles, the delivery of a homogeneous microwave magnetic field is critical in order to simultaneously perform this optimization across the entire area [14]. Such microwave homogeneity is also critical to pulse-based coherent quantum control protocols, such as Ramsey-type sequence, which can significantly increase the sensitivity to time-varying external magnetic field [3]. Homogeneous microwave *synchronously* rotate the spin states of a large number of NV centers on the Bloch sphere [15], [16]. Since the microwave-field strength determines the Rabi nutation frequency of each NV electron spin, spatial variation of the microwave field causes dephasing of the overall quantum ensemble.

Traditional microwave-launching structures include single straight wires [4], [13], metal loops [5], [7], [17], and split-ring resonators [15], [16]. They can only keep the field homogeneity in an area that is much smaller than the launcher size. That is undesired for compact chip implementation when excitation of a large-size diamond is pursued. Meanwhile, the above structures also have poor power-delivery efficiency, hence watt-level microwave input power is common [7], [15], [16]. We note the above solutions share one commonality in that they all rely on *one piece of passive structure driven by a single electrical port*. That, unfortunately, makes it extremely difficult, if not impossible, to synthesize a certain desired current distribution[1], because the only design variable is the structural geometry.

One distinct advantage of the implementation using integrated circuits is *the highly flexible and tight integration between passive and active components.* A large number of biased transistors, when forming current sources, can be used to mandate the complex current values at various particular locations on the passive structure (Fig. 4). Compared to the aforementioned passive-only structures, this new design

[1]For electrically small structures (size$\ll \lambda_{2.87GHz}$), the distributions of the current on the structure and the generated near-field magnetic wave follow a one-to-one mapping. Note that although displacement current also generates magnetic field, our following discussions are constrained to structures mainly with conduction current.

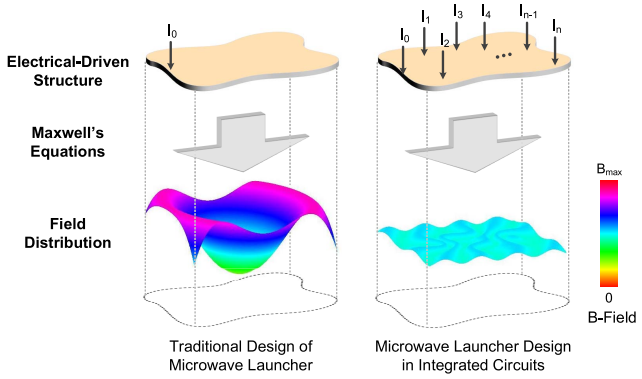

Fig. 4. Comparison of design methodologies for the microwave launcher in a quantum sensor. A distributed codesign of passive and active components is equivalent to adding more boundary conditions to an electromagnetic-solving problem, hence providing better control of the near-field pattern.

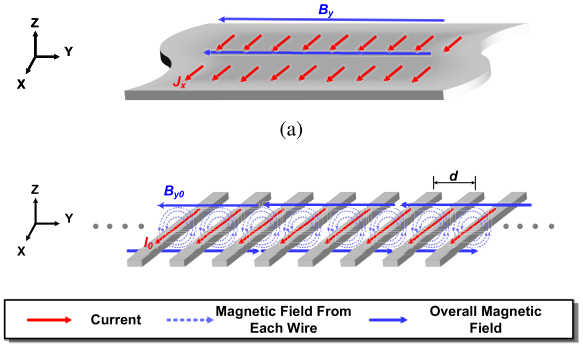

Fig. 5. Approaches to generate homogeneous magnetic field. (a) Infinite sheet of uniformly-distributed current. (b) Infinite array of wires with uniform driving current.

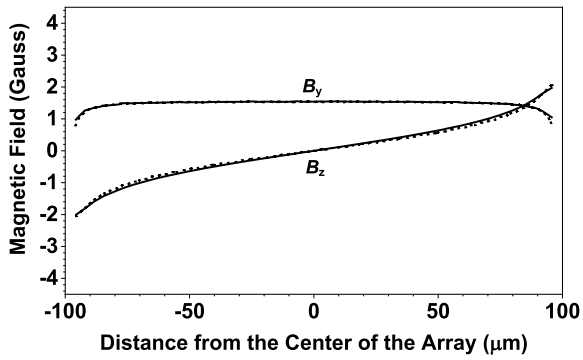

Fig. 6. Simulated and calculated field distribution ($f = 2.87$ GHz) of a wire array with uniform driving current ($I_0 = 1$ mA).

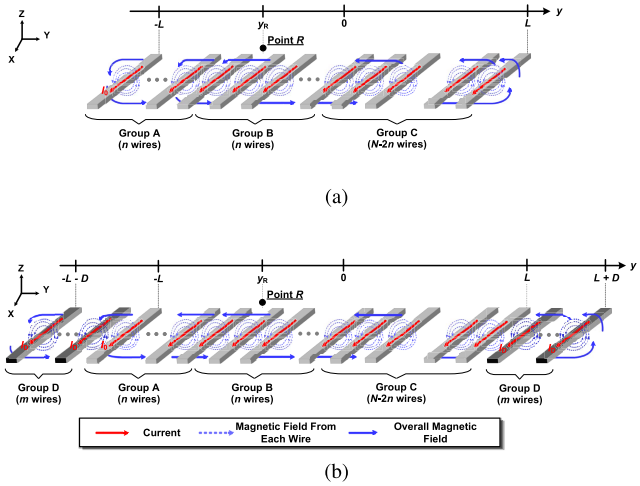

Fig. 7. (a) Finite array of wires with uniform driving current. (b) Additional pair of boundary wire arrays (Group D) for nulling the vertical magnetic field between $-L$ and $+L$.

methodology provides abundant additional degrees of freedom through the positions and currents of the embedded transistors. A finer control of near-field wave distribution is therefore much easier. Note that similar concepts were already proposed and applied to millimeter-wave and terahertz integrated circuit designs [18]–[20].

Following the above methodology, our microwave launcher design in Fig. 3 evolves from an ideal, infinite sheet of uniformly-distributed surface current density J_x (see Fig. 5(a)), which generates a homogeneous field B_y with a transverse (y-) direction and strength of $\mu_0 J_x/2$ (μ_0: permeability of vacuum). However, such current uniformity is hard to imitate in a single metal structure, due to the self-redistribution of current like skin effect. To prevent such redistribution, the current sheet is first transformed into an infinite array of wires, each driven by an identical current I_0 (Fig. 5(b)). With a tight wire center-to-center pitch d (or equivalent current density of I_0/d), a uniform transverse magnetic field can still be obtained, with a field strength of $\mu_0 I_0/2d$. The wire array also ensures high scalability in the longitudinal (x-) direction for large-area diamond.

In reality, only a finite wire array can be implemented. The introduced boundaries, however, break the above homogeneity. Fig. 6 shows the simulated field distribution of a 48-wire array with $d = 4$ μm. Although the transverse component of the field B_y maintains homogeneity, the vertical component B_z becomes nonzero and exhibits large gradient over y-axis. To understand that, we focus at a reference point (Point R) located above an array of N wires and closer to the left side (i.e. $y_R < 0$ in Fig. 7(a)). The wires are then divided into three groups: the n wires located between y_R and the left boundary $-L$ (Group A), another n wires symmetrically located at the right side of Point R (between y_R and $2y_R + L$, Group B), and the rest (Group C). Next, note that at Point R, the vertical magnetic fields generated by Group A and B cancel, and the B_z generated by Group C, by Ampere's Law, is

$$B_{z,C}(y_R) = -\frac{1}{2\pi}\int_{2y_R+L}^{+L} \frac{\mu_0 J_x dy}{y - y_R} = \frac{\mu_0 J_x}{2\pi} \ln \frac{L + y_R}{L - y_R} \quad (3)$$

where the discreteness of the array is approximated as a uniform current sheet with a current density of $J_x = I_0/d$. Note that (3) also applies for $y_R > 0$. Shown in Fig. 6, the result calculated from (3) well matches the simulation by HFSS [21]. Intuitively, $|B_z|$ increases toward the edges because the number of conductors in Group A and B decrease and the effect of the field due to the remaining Group C increases.

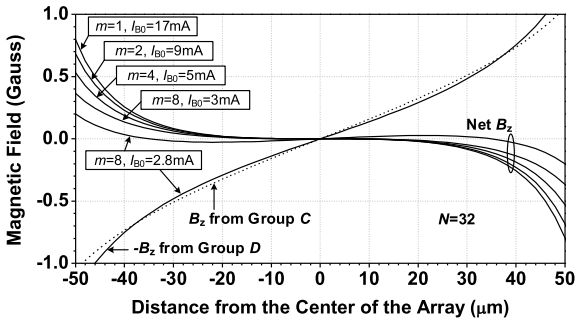

Fig. 8. Calculated profiles of vertical field generated by Group C and D (and the residue after the cancellation) of the array shown in Fig. 7. Note that the B_z of Group D is plotted with its polarity reversed, to facilitate a straightforward comparison with B_z from Group C.

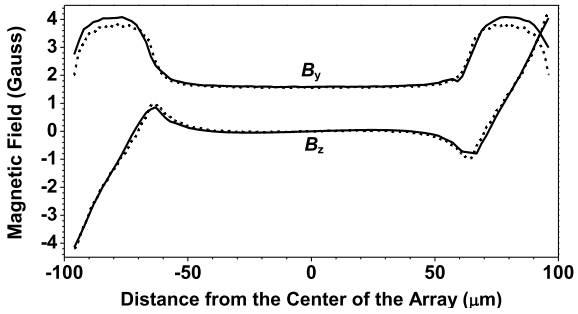

Fig. 9. Simulated (solid line) and calculated (dashed line) field distribution of the entire launcher wire array. Here, $f = 2.87$ GHz, $N = 32$, $m = 8$, $L = 64$ μm, $D = 32$ μm, $I_0 = 1$ mA, and $I_D \approx 3$ mA.

To create an opposite magnetic-field gradient for nulling the above B_z, a pair of additional m-wire arrays (Group D in Fig. 7(b)), which are driven by I_D per wire, are symmetrically placed at $y = -L-D$ to $-L$ and $y = L$ to $L+D$. Their combined impact on the vertical magnetic field at $y = y_R$ is derived as

$$B_{z,D}(y_R) = \int_{-L-D}^{-L} \frac{\mu_0 m I_D dy}{2\pi D(y_R - y)} - \int_{L}^{L+D} \frac{\mu_0 m I_D dy}{2\pi D(y - y_R)} = \frac{m\mu_0 I_D}{2\pi D} \ln \frac{(y_R + L + D)(L - y_R)}{(L + D - y_R)(y_R + L)} \quad (4)$$

of which some example plots (to be discussed more) are shown in Fig. 8, indicating the similarity of its curve shape to that from Group C. To further determine the value of I_D, we compare the derivatives of (3) and (4) around the center of the launcher

$$\frac{dB_z}{dy}|_{y=0} = \begin{cases} \dfrac{\mu_0 J_x}{\pi L} & \text{for Group } C \\ -\dfrac{\mu_0 m I_D}{\pi L(L+D)} & \text{for Group } D. \end{cases} \quad (5)$$

Therefore, for zero B_z around the array center, the value of I_D should be

$$I_{D,0} = \frac{L+D}{m} J_x = \frac{L+D}{md} I_0 = \left(1 + \frac{N}{2m}\right) I_0. \quad (6)$$

The last step of (6) assumes that the boundary arrays adopt the same wire pitch d as the N-wire uniform array in the center. For a 32-wire uniform array ($N = 32$) with $I_0 = 1$ mA and $d = 4$ μm, the vertical field $B_{z,D}$ generated by the boundary array pair with varying wire numbers m, as well as the residual of B_z after cancellation, are plotted in Fig. 8. We see that a larger m improves the area of uniformity at a modest expense of higher current consumption. Interestingly, if the I_D value is slightly lower than the one calculated by (6) (e.g. for $m = 8$, the calculated value for I_D is 3 mA), the B_z field around $y = 0$ is not canceled perfectly but the overall 95% uniformity area is extended to $y \approx \pm 40$ μm. Lastly, Fig. 9 shows the HFSS-simulated field distribution of the entire launcher ($N = 32$, $m = 8$, $d = 4$ μm) including the current return path, which is implemented at the Metal 8 (M8) interconnect layer of our chip prototype. The calculated profile in Fig. 9 is achieved with $I_D = 2.8 I_0$. Note that the HFSS simulation is done with a slightly larger I_D ($I_D = 3I_0$) to account for the uncalculated effect of current in the return path. Compared to Fig. 6, the overall homogeneity of the magnetic vector field is significantly improved.

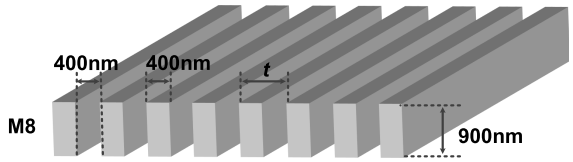

Fig. 10. Single-layer plasmonic grating filter implemented on Metal 8 [10].

C. Nano-Photonic Filter on CMOS

Plasmonic filters based on a multistacked-layer gratings in the back-end-of-line (BEOL) of CMOS technologies have been demonstrated previously in [22]. In our first CMOS quantum sensor [10], a single-layer filter based on the same principle of wavelength-dependent plasmonic loss is adopted. The filter is implemented at M8 with a grating pitch, t, of 800 nm. This filter exhibits a green-to-red rejection ratio of $\sim$10 dB in our experiment. Based on the discussion in Section II, that ratio should be improved to enhance the magnetometry sensitivity. Next, we show how a wavelength-dependent diffraction pattern under the plasmonic filter layer is utilized to achieve the goal. To facilitate that discussions, we first revisit some details related to the plasmonic grating layer.

Fig. 10 shows the structure of the filter used in [10] and [11]. Each slit is considered as a parallel plate waveguide transmitting light inside a dielectric (refractive index $\sqrt{\epsilon_d} \approx 1.5$) in the z-direction. The incoming light is modeled as a plane wave with a transverse electrical field E_x and a propagation constant $k_0 = \omega\sqrt{\epsilon_d}/c$ (c is the speed of light in vacuum). This light is coupled to the TEM mode of the parallel-plate waveguides, which has identical propagation constant k_0 (see Fig. 11(a)). As the propagating wave interacts with the metal, the surface plasmon polariton (SPP) mode at the metal-dielectric interface is excited. Note that the dispersion relation of SPP mode is

$$k_{z,\mathrm{SPP}} = \beta_{\mathrm{SPP}} + i\alpha_{\mathrm{SPP}} = k_0 \sqrt{\frac{\epsilon_m}{\epsilon_m + \epsilon_d}}. \quad (7)$$

In (7), the permittivity ($\epsilon_m = \epsilon_{mr} + i\epsilon_{mi}$) of the metal (copper in our case) has a negative real part, which leads to $\beta_{\mathrm{SPP}} > k_0$.

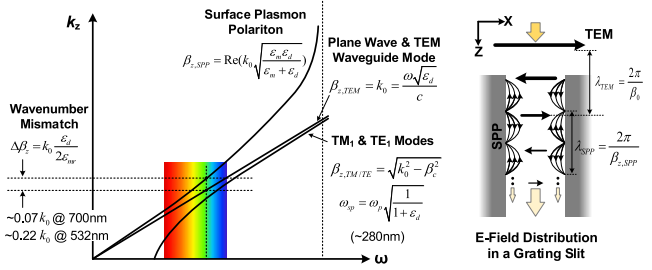

Fig. 11. TEM and SPP modes inside a grating slit (modeled as a parallel-metal-plate waveguide). (a) Dispersion relationships. (b) Short-distance coupling.

Although coupling from the TEM waveguide mode and the SPP mode generally does not occur[2], it still does in this case. That is because, by examining the value of β_{SPP} in (7)

$$\beta_{\text{SPP}} = \Re(k_0\sqrt{\frac{\epsilon_m}{\epsilon_m+\epsilon_d}}) \approx k_0\left(1-\frac{\epsilon_d}{2\epsilon_{mr}}\right) \tag{8}$$

we see that since $|\epsilon_{mr}|$ remains large, the relative mismatch between the β_{SPP} and $\beta_{\text{TEM}} = k_0$, namely $\epsilon_d/2\epsilon_{mr}$ in (8), are ~0.07 for red (700 nm) and ~0.22 for green (532 nm) (see Fig. 11(a)). These calculations are based on the Drude-Brendel–Bormann model [23], [24]. Along the vertical propagation distance of the grating (i.e. the M8 grating thickness $d = 900$ nm, or $2\lambda_{\text{red}} = 2.5\lambda_{\text{green}}$ in dielectric), the accumulated phase mismatch is

$$\Delta\phi = 2\pi\frac{\epsilon_d}{2\epsilon_{mr}}\frac{d}{\lambda} \tag{9}$$

or ~50° (red) and ~180° (green), respectively. Therefore, for red light, constructive coupling from the TEM mode to SPP mode still occurs within the single-layer grating. For green light, although phase mismatch appears to be large, the coupling is still effective in the M8 slit due to the large SPP loss; and when the TEM wave reaches the bottom half of the slit, its power is already heavily depleted. To quantify the loss of the SPP mode, we derive the attenuation factor α_{SPP} in (7)

$$\alpha_{\text{SPP}} = \Im\left(k_0\sqrt{\frac{\epsilon_m}{\epsilon_m+\epsilon_d}}\right) \approx k_0\frac{\epsilon_d\epsilon_{mi}}{2\epsilon_{mr}^2} \tag{10}$$

α_{SPP} exhibits large difference between red ($\approx 0.006k_0$) and green ($\approx 0.18k_0$) as calculated based also on the Drude-Brendel–Bormann model.

Using a finite-difference time-domain (FDTD) solver, Lumerical, we simulate the green-to-red suppression ratio due to the slit in M8 layer ($d = 900$ nm), which is ~9 dB (Fig. 12(a)). Increasing the slit thickness by stacking more grating layers (in M7, M6...) is expected to further increase the suppression of the green light [22]. However, that causes degradation of red-light transmission due to the scattering at the side walls formed by the sparse inter-layer via pillars.

[2]Normally, dedicated material/geometrical configurations, such as the Otto and Kretschmann-Raether configurations, are needed to enable the excitation of the SPP mode.

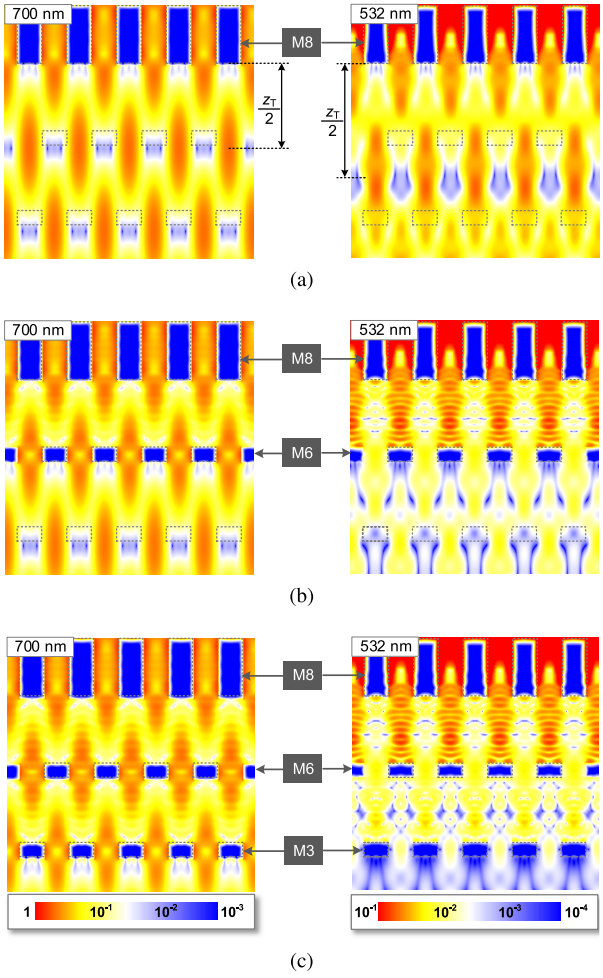

Fig. 12. Simulated FDTD Poynting vector profile $|P| = |E \times H|$ for (a) single-layer grating in M8, (b) double gratings in M8 and M6, and (c) triple-layer gratings in M8, M6 and M3. Note: the scale bar for green (right column) is 10× lower than that for red (left column), in order to count for the ~10-dB plasmonic loss in the M8 grating and to better show that the M6 and M3 gratings further suppress the transmission at 532 nm.

Moreover, as Section III-D describes, the grating structure in M8 is also used for the microwave wire array (Section III-B). Connecting it to the lower metal layers would significantly decrease the density and the uniformity of the RF current inside the wires. In our chip, an alternative approach based on the wavelength-dependent diffraction pattern of the grating is adopted.

As the simulation in Fig. 12(a) shows, the diffraction of the light coming out of the grating in M8 causes repeated self-imaging patterns in the chip dielectric. That optical phenomenon is called Talbot effect [25] and the vertical (z-) period of the self-images (i.e. Talbot length) is

$$z_T = \frac{\lambda}{1-\sqrt{1-\frac{\lambda^2}{t^2}}} \tag{11}$$

where λ is the wavelength in the dielectric and t is the grating period (800 nm in our case). For the red (700 nm) and green (532 nm) light, z_T is ~2.5 μm and ~3.4 μm (see Fig. 12(a)). That means we may strategically place additional metal structures at positions which are dark in red diffraction pattern

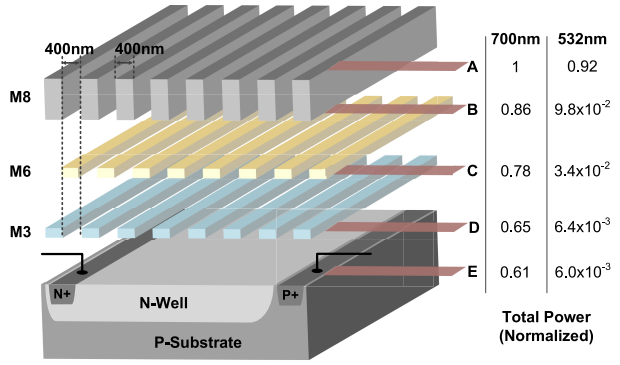

Fig. 13. Simulated transmission values through the filter. The total power is derived by surface integrals of Poynting vectors at varying depths of the chip.

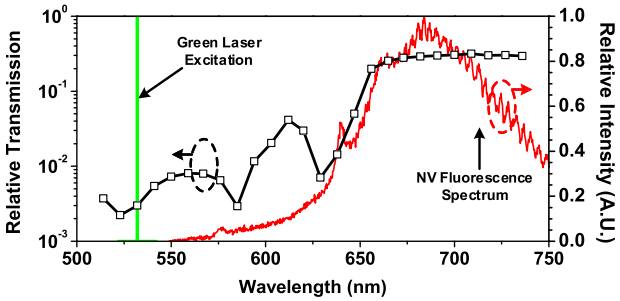

Fig. 14. Transmission through the filter at different wavelength.

(so that the light is not affected) but bright for green (so that the light is blocked). In the 65-nm CMOS process used for this work, the distance between M8 and M6 layers is close to the half Talbot length for red; therefore, a M6 grating with 400-nm strip width and spacing is placed. With the positions of the metal strips right under the slits of M8, the M6 grating has little interference with the red-light transmission, while blocking a significant portion of the green light (Fig. 12(b)). It is noteworthy that the similar multigrating concept was previously adopted for lensless 3-D CMOS cameras [26], where the angle sensitivity of the structure is utilized. To the authors' best knowledge, this is the first time in CMOS that the idea of diffraction selectivity is applied into optical spectral filtering.

Following the same principle, a third grating layer in M3, of which the distance to M8 is about one Talbot length at 700 nm, is added to further enhance the green-light rejection (Fig. 12(c)). The same grating strip width and spacing of 400 nm are used. Fig. 13 provides the normalized transmitted power (Poynting vector integrated over a x-y cross-sectional area) at varying chip depths. For green light, the plasmonic behavior attenuates the power by 9.7 dB, and the M6 and M3 gratings pose an additional 12.1 dB loss, leading to a total attenuation of 21.8 dB. Meanwhile, the total insertion loss for red light is only 2.1 dB. Note that the reflection loss at the top of M8, which is ~3 dB due to the 50% metal fill factor, is not included in both cases. Lastly, the simulated transmission response (excluding the 50% surface reflection) of the filter from 500 nm to 750 nm is plotted in Fig. 14. The spectrum of the NV-center red fluorescence is also shown. It can be seen that the majority of the fluorescence power between 650 and 725 nm is transmitted efficiently to the photodiode beneath the filter.

In general, the topmost layer of the filter should be as thick as possible and the separation between the metal lines should be as small as possible to increase the coupling to the plasmonic mode, hence larger green rejection. Note that there is normally a tradeoff between the above two parameters due to the limited aspect ratio in CMOS technologies. The lower metal layers have to be placed in alignment with the maxima of the green and the minima of the red diffraction patterns. The vertical distance between metal layers in many CMOS processes is sufficient for the above requirement, although that in some more advanced technology nodes may not.

D. Co-Design of the Circuits, Microwave Launcher, and Photonic Filter

The full schematic of the microwave launcher with the switches and current sources banks is shown in Fig. 15. NMOS current mirrors are used to control the current in each individual wire of the array. PMOS switches are used to convert the rail-to-rail square-wave output voltage of the PLL into microwave square-wave currents in the array. It is worth mentioning that the higher harmonics of the square-wave microwave field is not sensed by the NV centers. Only the fundamental component ~2.87 GHz dominates the operation of driving the electronic transitions. The current sources are designed to enable microwave square-wave current (I_0) control from 0.1 to 1 mA. This corresponds to microwave field strength of 0.1 Gauss to 1 Gauss.[3]

At low current values our simulation in Fig. 16 indicates that when the PMOS switches are off, the current of wire returns to zero at a slow speed. This is due to the parasitic capacitance of the wire array, the transistors in the current sources and switches, as well as the limited discharging current. The parasitic capacitance is estimated to be ~5 fF from Fig. 16, assuming a linear discharging current of 0.1 mA flowing in each wire. To increase the pull down speed, a row of NMOS switches are also used (see Fig. 15) to provide a fast discharging (see the comparison in Fig. 16). The transistors dimensions (W_1/L_1, W_2/L_2, and W_3/L_3) are scaled up by a factor of 3 at the boundaries. As described in Section III-B, the microwave launcher is implemented on M8 with wire width and spacing of 2 μm. Therefore, all the transistor layouts are designed in a multiplier fashion so that they can fit in the tight wire pitch. In addition, the layout of the transistors is fully symmetric to minimize the mismatch. A pair of wide return ground paths are used to close the current loop.

Part of the photonic filter is also implemented on M8 with unit width and spacing of 400 nm (shown in Fig. 13). The smallest dimension limited by the design rule of the technology is selected to enhance the coupling to the SPP mode.

[3]Note that the I_0 used in Section III-B refers to the current of a sinusoidal wave at $f_0 \approx 2.87$ GHz. To be consistent with the values given here, the simulated/calculated magnetic-field strength in Fig. 9 should be multiplied by a factor of $2/\pi$ to count for the amplitude difference between a square wave and its fundamental sinusoidal component.

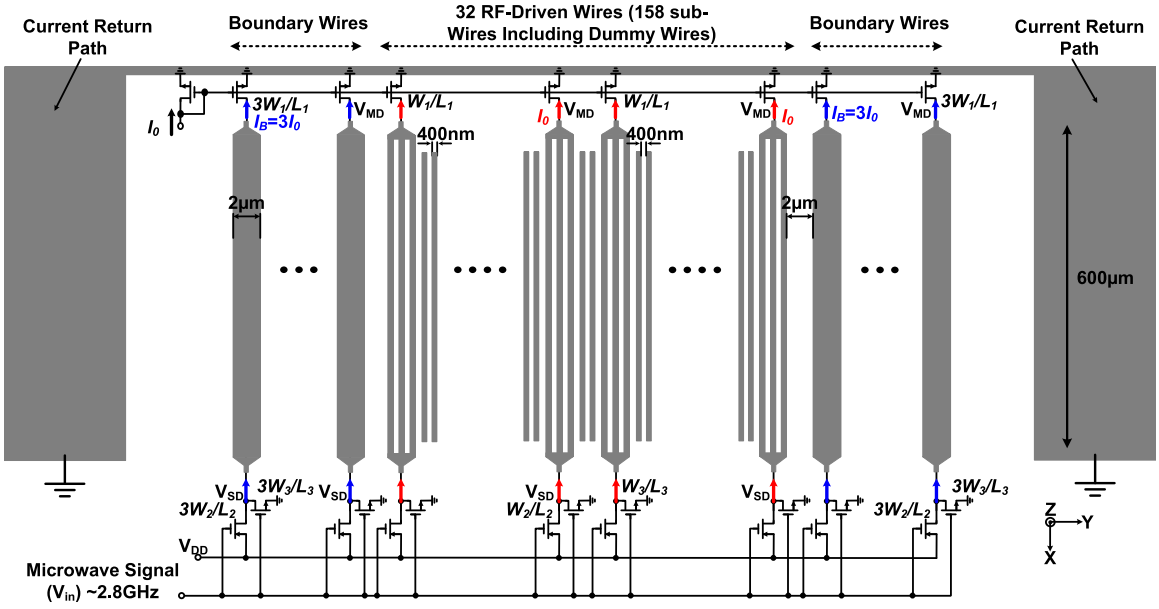

Fig. 15. Schematic of the microwave launcher with the switches and the current sources.

To cater the needs of both components, shown in Fig. 15, each of the microwave launcher wires other than the boundary wires is divided into three sub-wires with their two ends electrically connected. The width and the spacing of these sub-wires are 400 nm. In addition, each of the 2 μm spacing in the microwave launcher is filled with another two electrically floating dummy wires with 400-nm width and spacing (Fig. 15). These dummy wires do not affect the microwave generation/delivery operation, but along with the other sub-wires, they form the desired photonic filter geometry. The metal gratings implemented at M6 and M3 are also electrically floating and have very small thickness ($\sim$0.2 μm). Therefore, the eddy currents generated due to the microwave field in the horizontal direction is negligible and does not affect the uniformity of the microwave field. In the current design, the local metal density rules around the sensing area are waived. The filter area is 350×130 μm^2. In this prototype, we implement blocking walls around the photodiode area and a conservative size was adopted for the sensing area, to minimize the leakage of light into the photodiode. The size of the photodiode placed under the filter is 300×80 μm^2. In future designs, the photodiode area may increase for better SNR.

This array generates $>$95% field homogeneity over $\sim$ 50% of its area compared to 25% in [10]. Uniform array spacing is adopted in this design, however, in Section V, we show that a certain gap between group D and group A/C can achieve homogeneity across a larger area. The design is only enabled by CMOS technologies, where we can integrate a very tight wire array with efficient switching and current control.

E. ON-*Chip Synthesis of the Microwave Frequency*

A PLL loop is used to stabilize the output of the voltage-controlled oscillator (VCO) that drives the NV centers. The full schematic of the PLL is shown in Fig. 17. To ensure a uniform phase of the magnetic field across the wire array,

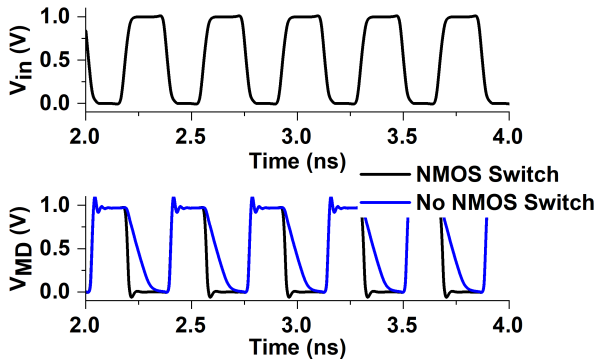

Fig. 16. Comparison between the switching performance with and without extra NMOS switch. The first plot shows the input microwave signal (V_{in}) and the second one shows the voltage at the drain of the NMOS current source (V_{MD}).

the VCO is based on a tightly coupled ring-oscillator array. Four sub-oscillators are placed with a spacing of $\sim$50 μm (see Fig. 3). The two oscillators in the middle drive 32 wires, while the other two oscillators on the array boundaries drive eight wires each. Compared to a centralized signal-generation scheme, the coupled-oscillator eliminates the phase variation caused by different lengths of the microwave-distributing traces. In addition, careful placement and routing are done to ensure uniform phases at the wire array. Our simulations show that the uniformity of the horizontal component of the microwave field (B_y) is $>$95 % for 5° random phase mismatch, which is the expected maximum phase mismatch at the wire array inputs. Here, ring oscillators, instead of LC oscillators, are chosen, in order to eliminate the need for extra inductors, as well as any magnetic coupling and degradation of field homogeneity in the diamond-sensing area. A ring oscillator also offers wider tuning range and layout compactness. Its inferior phase noise is improved by 6 dB due

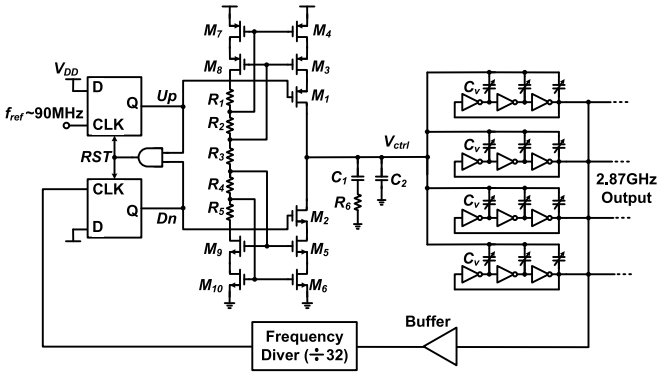

Fig. 17. Schematic of the 2.87-GHz PLL.

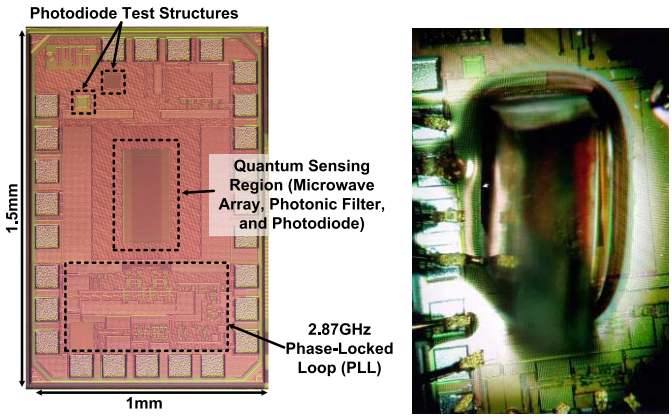

Fig. 18. (a) Micrograph of the CMOS quantum magnetometry chip. (b) Chip with a diamond placed on the top.

to the oscillator coupling, and in fact our analysis indicates that our sensor sensitivity is currently limited by the green and red light noise, as explained in Section IV-B. The VCO frequency is tuned using varactors ($C_v = 9$–42 fF) with a coefficient of 1.2 GHz/V. The charge pump current of the PLL is 5 mA and the loop filter parameters are $C_1 = 1$ nF, $R_6 = 220\ \Omega$, and $C_2 = 20$ pF.

IV. Chip Prototype and Experimental Results

The chip prototype is fabricated using a TSMC 65-nm CMOS technology. The chip micrograph is shown in Fig. 18(a). The chip has an area of 1×1.5 mm^2 and consumes 40 mW of power. In the experiment, the amplitude of the square wave current in the microwave launcher (I_0 in Fig. 18(a)) is set to 0.5 mA, which corresponds to 0.5 Gauss of microwave field strength. This field efficiently couples to a diamond slab with NV centers placed and attached directly onto the top of the CMOS chip as shown in Figs. 3 and 18(b). This diamond is a single crystalline CVD-grown diamond from Element 6. It is electronically irradiated with a dosage of 10^{18} e$^-$/cm^2 at 1 MeV, and then annealed for 2 h at 850 °C. This results in 0.01 ppm of NV density in the diamond. Immersion oil is used to adhere the diamond slab to the chip. By bridging the difference of the refractive index, the oil also minimizes the fluorescence loss. The measured filter rejection for green light (532 nm) is ~25 dB, which well matches the simulation results in Section III-C. We measure the green light rejection of the filter using two test photodiodes as shown in Fig. 18(a). One of them is covered by the photonic filter. Then we compare the output current in both cases at the same laser intensity level. A 45° cut is introduced in the diamond's corner to direct the vertical incident green laser horizontally to further enhance the overall green rejection ratio to ~33 dB. The extra green light rejection is measured by comparing the output current of the photodiode due to the green laser with and without diamond slab. The measured responsivity of the ON-chip photodiode is 0.19 A/W at the green laser wavelength (532 nm). This corresponds to a quantum efficiency of 45%.

A. Optical Detected Magnetic Resonance Measurements

The measurement setup to generate the ODMR spectral line is shown in Fig. 19(a). A 532-nm gaussian laser beam is used to excite the NV centers in the diamond. The laser beam diameter and power are 100 μm and 200 mW, respectively. This corresponds to 40 μA of current due to the green laser pump. The beam is focused on the diamond slanted edge, which then directs it horizontally. The red fluorescence detected by the ON-chip photodiode is recorded while sweeping the reference signal (~90 MHz) of the ON-chip PLL. Due to the limited green-red suppression ratio of the ON-chip filter, the red fluorescence signal is still superposed on a large green-light background at the output of the photodiode. Meanwhile, we notice the green-light excitation exhibits large power fluctuation, so to remove the fluctuating background signal, a frequency-modulation (FM) scheme is used, where the chip-generated microwave probing frequency $f_p(t)$ is periodically varied with a deviation of 6 MHz and repetition frequency f_m of 3 kHz. That is done by modulating the ~90-MHz reference signal of the ON-chip PLL. As shown in Fig. 19(b), the corresponding photodiode output changes at f_m (with harmonics at $2f_m$, $3f_m$, etc.), which is then readily measured by a lock-in amplifier (SR865) with the reference at f_m. The lock-in amplifier also provides narrow-band filtering around f_m. Note that the FM technique is common in spectroscopy [27] and atomic/molecular clocks [28]. Lastly, to further de-embed the excitation noise within the lock-in amplifier bandwidth, a differential detection scheme is adopted, where a split beam of the same laser is measured by an OFF-chip photodiode; such a duplicated noise signal is then taken by the lock-in amplifier and is subtracted from the chip output. Two identical OFF-chip resistive transimpedance amplifiers (TIA) with transimpedance gain of 10 kΩ are used to convert the photodiode currents into voltage. This gain is chosen to prevent the saturation of the amplifier due to the green current background (40 μA).

First, without an externally applied magnetic field, an ODMR plot is obtained as shown in Fig. 20(a). A strong spin resonance, which results from all four NV centers in the diamond lattice, is detected at 2.87 GHz. The FM technique introduced previously can be interpreted as taking the first-order derivative of the regular Gaussian-shape transition line; as a result, the measured curve has the zigzag shape

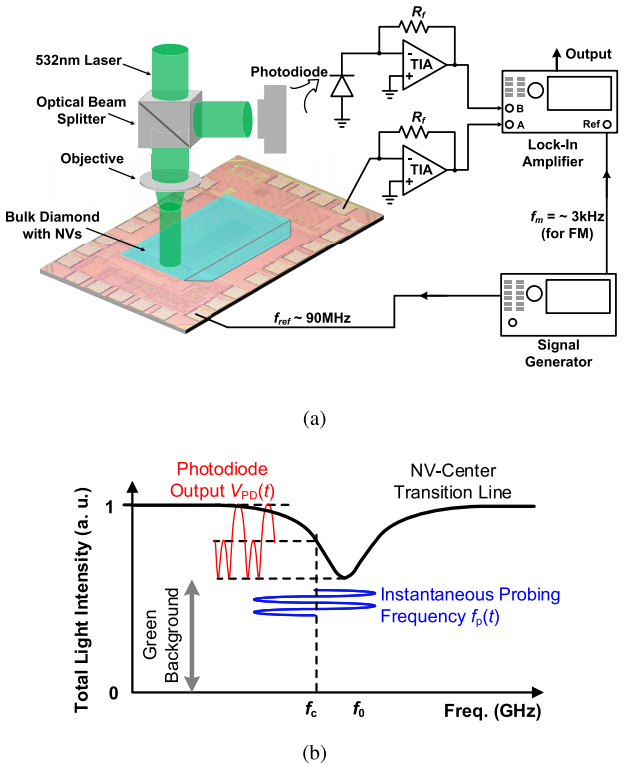

Fig. 19. (a) Test setup for the hybrid NV-CMOS magnetometer. (b) FM scheme used in the setup.

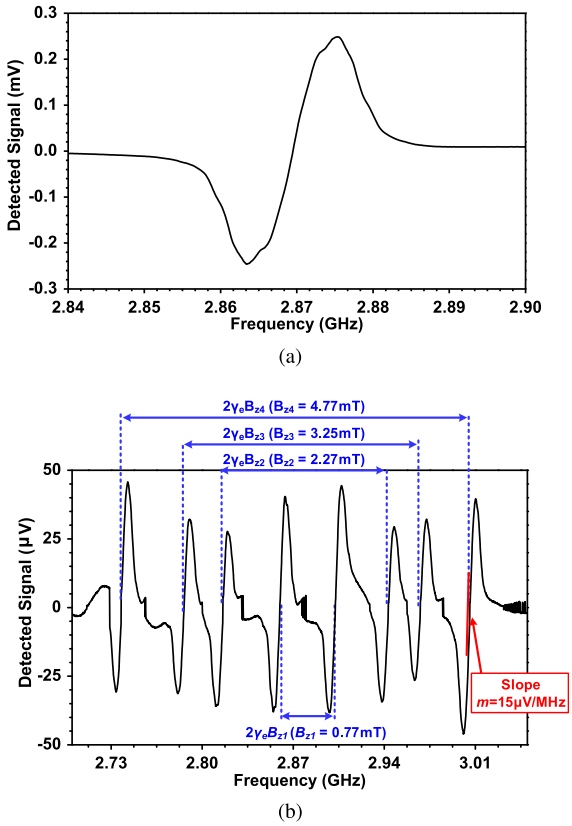

Fig. 20. Measured ODMR plot from the CMOS chip, when (a) no external magnetic field is applied, and (b) 5.4-mT external magnetic field is applied from a certain angle.

shown in Fig. 20(a). The zero-crossing point corresponds to the actual transition frequency. Next, a 5.4-mT dc magnetic field is applied to the sensor from a nearby permanent magnet. This results in the Zeeman splitting for the spin states of the NV centers. As shown in the measured ODMR plot in Fig. 20(b), four pairs of resonances are observed. They correspond to the four NV-center orientations of the single crystalline diamond. The difference of the transition frequencies (i.e. zero-crossing points) in each resonance pair is proportional to the external static magnetic field along the associated NV-center orientation. The proportionality constant, as described in Section II, is $\gamma_e = 28$ GHz/T. Accordingly, the magnetic fields along the four NV-center orientations are 0.77, 2.27, 3.25, and 4.77 mT, respectively. Lastly, as the comparison between Fig. 20(a) and (b) shows, the chip output signal with external magnetic field is reduced due to the breaking of the degeneracy of the resonances from 2.87 GHz. Fig. 20 clearly indicates that, by mapping the projections of the external magnetic field along the four NV-center orientations and certain frame of reference, one can construct the full vector magnetic field.

One practical way to use the sensor for vector-field sensing, is to first "bias" the sensor with a static magnetic field (e.g. a permanent magnet), which allows for the four resonances to be completely split (such as shown in Fig. 20(b)). Then, we record the additional change of the sensor output voltage $\Delta v_{\text{out},i}$ ($i = \pm1, \pm2, \pm3, \pm4$) around each zero-crossing point of the FM-based ODMR curve. Note that $\Delta v_{\text{out},i}$ is caused by the shift of each resonance frequency Δf_i due to the projection of the added field on the associated NV-center axis ΔB_{zi} (to be measured) on top of the bias static field, its expression is (for positive i)

$$\Delta v_{\text{out},i} = m\Delta f_i = m\gamma_e \Delta B_{zi} \tag{12}$$

where m is the slope of the ODMR curve at each transition zero-crossing point (~15 μV/MHz in our case, see Fig. 20(b)). The value of ΔB_{zi} can be derived from $\Delta B_{zi} = \Delta v_{\text{out},i}/(m\gamma_e)$. Note that the transition frequencies of both $|m_s = \pm1\rangle$ sub-levels are also temperature dependent (with a coefficient of -74 kHz/K [29]). To cancel such temperature-induced drifts, it is better to measure the differential change of each pair of $|m_s = \pm1\rangle$ transitions, and use the following equation for ΔB_{zi} [11]:

$$\Delta B_{zi} = \frac{\Delta v_{\text{out},i} - \Delta v_{\text{out},-i}}{2m\gamma_e} \quad (i = 1, 2, 3, 4). \tag{13}$$

B. Magnetic Sensitivity Estimation

In order to calculate the magnetic sensitivity of the sensor, the noise floor, σ (unit: V/Hz$^{1/2}$), is measured. The sensor noise is measured by monitoring the read-out of noise in the lock-in amplifier while sweeping the modulation frequency f_m. The results are shown in Fig. 21, where the sensor noise floor is ~0.1 μV/Hz$^{1/2}$. The noise below 3 kHz is mainly flicker noise. However, there are some points where the noise peaks abruptly. Those are caused by the interference from the unshielded testing environment. This does not affect the noise performance of the sensor, since we are only interested

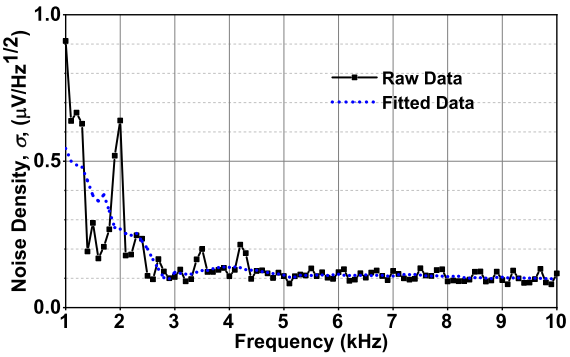

Fig. 21. Measured output noise floor of the sensor.

in the noise around f_m (3 kHz) due to the lock-in detection used in the experiment. The magnetometer sensitivity S (unit: T/Hz$^{1/2}$), which is the minimum detectable magnetic field with 1-s integration time, is calculated using the following equation:

$$S = \frac{\sigma}{\gamma_e m}. \tag{14}$$

The measured magnetometry sensitivity of this sensor at $f_m = 3$ kHz is 245 nT/Hz$^{1/2}$.

The sensor performance is limited by the green light fluctuations and the thermal noise of the TIA. The theoretical magnetic sensitivity (S_{th}) of the sensor can be estimated using the following:

$$S_{\text{th}} = \frac{\sigma_{\text{th}}}{\gamma_e m} = \frac{\sqrt{2(\bar{V}_{n_g}^2) + \bar{V}_{n_r}^2 + 2(\bar{V}_{n_t}^2)}}{\gamma_e m} = \frac{\sqrt{2(2qi_gR_f^2) + 2qi_rR_f^2 + 2(4KTR_f)}}{\gamma_e m} \tag{15}$$

where σ_{th} is the theoretical noise limit due to the green light shot noise ($\bar{V}_{n_g}^2$), the red fluorescence shot noise ($\bar{V}_{n_r}^2$) and the TIA thermal noise ($\bar{V}_{n_t}^2$) referred at the output of the TIA. For the first term of σ_{th}, q is the electronic charge, i_g is the current measured at the photodiode due to the green light ($\sim$40 μA), and R_f is the feedback resistor of the TIA (10 kΩ). i_r in the second term of σ_{th} represents the detected red fluorescence current by the photodiode. This current i_r equals ($V_{\max}/CR_f$), where $V_{\max}$ is the maximum voltage ($\sim$45 μV) of the ODMR curve in Fig. 20, and C is the ODMR contrast of $\sim$ 0.01. Therefore, i_r equals 450 nA. In the third term of σ_{th}, we assume that the TIA output referred noise is mainly limited by the feedback resistor R_f, K is the Boltzmann's constant, and T is the temperature. The factor of 2 used in the first and third terms of σ_{th} is due to the addition of the noise power from the two detection branches. Based on (15), the calculated theoretical sensitivity value is $\sim$150 nT/Hz$^{1/2}$, which agrees to a good extent with the measured value, and the difference is due to the residual un-canceled green light fluctuation. Even though this differential measurements technique increase the total shot noise limit by a factor of $\sqrt{2}$, it helps in canceling almost all the external laser fluctuation, which is almost one order of magnitude larger than the shot noise limit in our case.

Moreover, $\bar{V}_{n_g}$, $\bar{V}_{n_r}$, and $\bar{V}_{n_t}$ in (15), equal 36 nV/Hz$^{1/2}$, 3.8 nV/Hz$^{1/2}$ and 12 nV/Hz$^{1/2}$, respectively. This confirms that the contribution of the green light shot noise is the dominant source of noise in our system. We also estimated the magnetic sensitivity S_m due to the amplitude noise converted from the microwave generator spectral purity, using the following equation (detailed derivation given in Appendix A):

$$S_m = \frac{\sigma_m}{\gamma_e m} \approx \frac{2\pi f_m \phi_n m}{\gamma_e m} \approx \frac{2\pi f_m \phi_n}{\gamma_e} \tag{16}$$

where m is the slope of the FM-ODMR curve, and ϕ_n is the PLL phase noise (with a measured value of -88 dBc/Hz) at an offset equal to the FM modulation frequency ($f_m = 3$ kHz). The magnetic sensitivity calculated from (16) is $\sim$30 pT/Hz$^{1/2}$, which is much smaller than that from (15) and confirms that the PLL noise does not limit the sensitivity.

V. Conclusion

In this article, we present a vector-field magnetometer, which is based on a CMOS chip-scale platform with a hybrid integration of color centers (NV centers) in diamond. The chip consists of the essential components for manipulation and detection of the spin states of the NV centers in diamond. We demonstrate room-temperature magnetic field sensing with a sensitivity of 245 nT/Hz$^{1/2}$, which is 130$\times$ better than our previous prototype [11]. This enhancement is mainly due to the following: 1) the microwave launcher with uniform microwave generation that can be scaled up for large diamond area (i.e. large SNR). The area in this work increases by $\sim$10$\times$, resulting in $\sim$10$\times$ better SNR; 2) an enhanced multilayer nanophotonic filter for lower background noise. The green rejection is enhanced by $\sim$20$\times$. This translates to $\sim \sqrt{20}\times$ or 4$\times$–5$\times$ less green shot noise; and 3) the extra $\sim$10$\times$ rejection of the external laser fluctuation due to the differential measurement. It is important to note that, the direct comparison between the two systems is not straightforward, due the discrepancies between the two test setups. For instance, less laser pump power is used in this scalable prototype (200 mW) compared to the one in [11] (500 mW), and there is an extra $\sim \sqrt{2}\times$ increase of readout-circuitry noise due to the two paths used in the differential measurement presented in this article. Table I shows a summary of the performance in comparison with our previous prototype.

The scalable architecture and component designs presented in this article provide a clear pathway to further push the sensitivity of the proposed sensor to sub-nT/Hz$^{1/2}$. This is shown in Fig. 22, which plots the estimated sensitivity with varying optical filtering performance, sensing areas, and NV-centers densities (see Appendix B for more details). We predict that if the NV density reaches 1 ppm with a sensing area of 1 mm^2, the sensitivity can reach $\sim$600 pT/Hz$^{1/2}$. Toward achieving a compact highly sensitive CMOS quantum magnetometer, the green light pump can be integrated into the system using a chip-scale laser diode [30], or a green vertical-cavity surface-emitting laser (VCSEL) [31].

Further improvements can be done on the component level. For instance, better optimized configuration of the boundary wire arrays (i.e. Group D in Fig. 7(b)) used in the microwave

TABLE I
SUMMARY OF THE HYBRID CMOS-NV MAGNETOMETER PERFORMANCE AND COMPARISON WITH THE PRIOR ART

References	CMOS Process	Microwave Launcher	Photonic Filter	Overall Green Light Rejection †	Sensing Area	Vector Field Sensing	Sensitivity
This Work	65 nm	Wire Array (Scalable)	Three-Layers (Plasmonic &Talbot Effect)	33 dB	80 μm × 300 μm	Yes	245 nT/Hz$^{1/2}$
[11] Nature Elec.'19	65 nm	Loop Inductor (Non-Scalable)	One-Layer (Plasmonic Effect)	20 dB	50 μm × 50 μm	Yes	32 μT/Hz$^{1/2}$

†The overall green rejection due to the on-chip filter and the diamond cut.

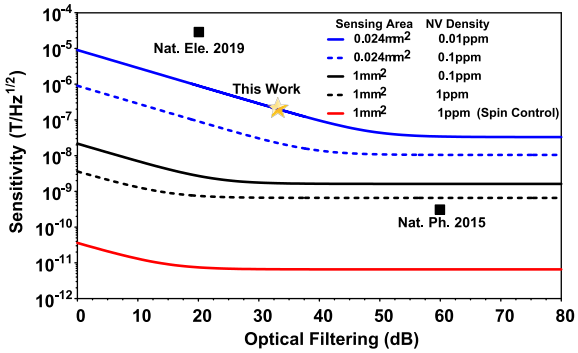

Fig. 22. Estimation of sensitivity for hybrid CMOS-NV magnetometers with different configurations.

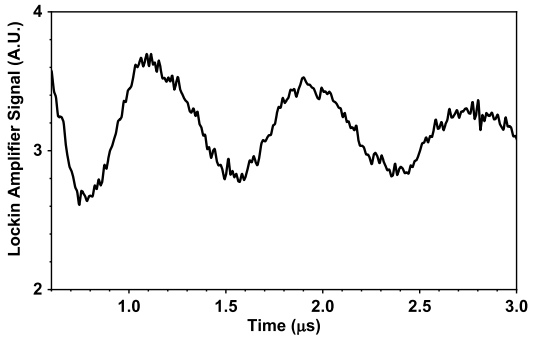

Fig. 23. Measured Rabi oscillations of an ensemble of NV centers using the unifrom microwave field generated by the chip.

launcher can lead to high magnetic homogeneity over a larger proportion of the total launcher area. For example, we find that if each Group D consists of $m = 4$ wires ($d = 4$ μm) with $I_D = 6.35$ mA, and a gap of 12 μm exists between Group D and Group A/C, 95% magnetic homogeneity is achieved for the entire -60–60 μm space above Group A-B-C. Homogeneity over large space also promises a significant sensitivity enhancement via spin-controlled pulse sequence [32]. It is worth mentioning that we have conducted pulse-based spin control experiments (e.g. Rabi oscillations [33]) on the whole NV ensemble using the magnetic field generated by the chip and OFF-chip optical detection. The measured Rabi oscillation, shown in Fig. 23, confirms that all the NV centers in the ensemble exhibit the same Rabi frequency (∼1.2 MHz) determined by the local microwave field and that the NVs are flipped at the same rate and their spin-dependent fluorescence signals add coherently. Lastly, the ability to manipulate the NV centers over a larger area also enables the integration of larger numbers of detectors for gradient magnetometry, multiplexed analytical nuclear-magnetic resonance (NMR) spectroscopy [34], atomic gyroscopes [35], and other quantum-sensing applications [36].

APPENDIX A
ESTIMATION OF THE CONTRIBUTION OF THE MICROWAVE PHASE NOISE ON THE SENSOR SENSITIVITY

The microwave signal that drives the NV centers can be represented as

$$V_{\mathrm{RF}} = V_0 \cos\left(\omega_0 t + \phi_n(t)\right) \tag{17}$$

where V_0 and ω_0 are the microwave signal amplitude and frequency, respectively. $\phi_n(t)$ is the phase noise of the microwave frequency. The instantaneous frequency can be represented as

$$\omega(t) = \omega_0 + \frac{d\phi_n(t)}{dt}. \tag{18}$$

The frequency fluctuations around the operating frequency (ω_0) is related to the phase noise by

$$\delta\omega = \frac{d\phi_n(t)}{dt}. \tag{19}$$

In our case, a lock-in amplifier is used to observe the noise around the modulation frequency (ω_m). Therefore, $\phi_n(t) = \phi_n \cos 2\pi f_m t$ can be assumed to have a sinusoidal form, where ϕ_n is the phase noise of the microwave source at the modulation frequency (f_m) in dBc/Hz. This means the peak frequency fluctuation is $\approx 2\pi f_m \phi_n$. Therefore, the voltage spectral density due to the PM to AM noise conversion is represented as

$$\sqrt{\frac{\bar{V}_n^2}{\delta f}} \approx 2\pi f_m \phi_n m \tag{20}$$

where m is the slope of the FM curve in V/Hz.

APPENDIX B
ESTIMATION OF SENSITIVITY FOR FUTURE HYBRID CMOS-NV MAGNETOMETERS

The sensor sensitivity is inversely proportional to the SNR of the sensor output

$$S \propto \frac{1}{\mathrm{SNR}} = \frac{\sigma_i \cdot \Delta\nu}{\gamma_e \cdot I_r} \tag{21}$$

where σ_i is the total noise current density (unit: A/Hz$^{1/2}$), $\Delta\nu$ is the linewidth of the ODMR curve, I_r is the photo-current due to the red fluorescence signal, and γ_e is 28 GHz/T. From our experiments, the linewidth of the ODMR is 6 MHz. The noise is limited by the shot noise of either the green excitation (for low optical filtering ratio) or the red fluorescence (for high optical filtering ratio)

$$\sigma_i = \sqrt{2 \cdot q \cdot (I_g + I_r)} \tag{22}$$

where q is the electronic charge, and I_g and I_r are the photo-currents due to the unfiltered green light and red fluorescence, respectively. The value of I_g is estimated as

$$I_g = P_g \cdot R_{\text{PD}} \cdot \eta_g \tag{23}$$

where P_g is the input optical power, R_{PD} is the photodiode responsivity, and η_g is the green rejection of the optical filter. The value of I_r is proportional to the total number n_{nv} of NV centers in the diamond, which is proportional to the sensing area A_{nv} and NV density ρ_{nv}. Lastly, the performance using the spin-controlled pulse sequence is estimated based on the fact that the equivalent transition linewidth (hence the zero-crossing slope m) of the configuration is reduced by $\sim$100$\times$ for ac magnetic field measurements [3], [32].

ACKNOWLEDGMENT

The authors would like to thank X. Yi, D. Kim, D. Bono, and C. Peng at MIT for technical discussions and their assistance during prototyping and testing.

REFERENCES

[1] A. Gruber, A. Dräbenstedt, C. Tietz, L. Fleury, J. Wrachtrup, and C. von Borczyskowski "Scanning confocal optical microscopy and magnetic resonance on single defect centers," *Science*, vol. 276, no. 5321, pp. 2012–2014, Jun. 1997.

[2] G. Balasubramanian *et al.*, "Nanoscale imaging magnetometry with diamond spins under ambient conditions," *Nature*, vol. 455, no. 7213, pp. 648–651, Oct. 2008.

[3] J. M. Taylor *et al.*, "High-sensitivity diamond magnetometer with nanoscale resolution," *Nature Phys.*, vol. 4, no. 10, pp. 810–816, Oct. 2008.

[4] D. Le Sage *et al.*, "Optical magnetic imaging of living cells," *Nature*, vol. 496, no. 7446, pp. 486–489, 2013.

[5] S. Steinert *et al.*, "Magnetic spin imaging under ambient conditions with sub-cellular resolution," *Nature Commun.*, vol. 4, no. 1, pp. 1–6, Jun. 2013.

[6] T. Wolf *et al.*, "Subpicotesla diamond magnetometry," *Phys. Rev. X*, vol. 5, no. 4, Oct. 2015, Art. no. 041001. [Online]. Available: https://link.aps.org/doi/10.1103/PhysRevX.5.041001

[7] H. Clevenson, M. E. Trusheim, T. Schroder, C. Teale, D. Braje, and D. Englund, "Broadband magnetometry and temperature sensing with a light trapping diamond waveguide," *Nature Phys.*, vol. 11, no. 5, pp. 393–398, 2015.

[8] D. B. Bucher, D. R. Glenn, H. Park, M. D. Lukin, and R. L. Walsworth, "Hyperpolarization-enhanced NMR spectroscopy with femtomole sensitivity using quantum defects in diamond," *Phys. Rev. X*, vol. 10, no. 2, 2018, Art. no. 021053.

[9] Y. Schlussel *et al.*, "Wide-field imaging of superconductor vortices with electron spins in diamond," *Phys. Rev. A, Gen. Phys.*, vol. 10, no. 3, Sep. 2018, Art. no. 034032. [Online]. Available: https://link.aps.org/doi/10.1103/PhysRevApplied.10.034032

[10] M. I. Ibrahim, C. Foy, D. Kim, D. R. Englund, and R. Han, "Room-temperature quantum sensing in CMOS: On-chip detection of electronic spin states in diamond color centers for magnetometry," in *Proc. IEEE Symp. VLSI Circuits*, Honolulu, HI, USA, Jun. 2018, pp. 249–250.

[11] D. Kim, M. I. Ibrahim, C. Foy, M. E. Trusheim, R. Han, and D. R. Englund, "A CMOS-integrated quantum sensor based on nitrogen–vacancy centres," *Nature Electron.*, vol. 2, no. 7, pp. 284–289, Jul. 2019.

[12] M. I. Ibrahim, C. Foy, D. R. Englund, and R. Han, "A scalable quantum magnetometer in 65nm CMOS with vector-field detection capability," in *IEEE Int. Solid-State Circuits Conf. (ISSCC) Dig. Tech. Papers*, San Francisco, CA, USA, Feb. 2019, pp. 458–460.

[13] A. Dréau *et al.*, "Avoiding power broadening in optically detected magnetic resonance of single NV defects for enhanced DC magnetic field sensitivity," *Phys. Rev. B, Condens. Matter*, vol. 84, no. 19, pp. 1–8, Nov. 2011.

[14] E. R. Eisenach, J. F. Barry, L. M. Pham, R. G. Rojas, D. R. Englund, and D. A. Braje, "Broadband loop gap resonator for nitrogen vacancy centers in diamond," *Rev. Sci. Instrum.*, vol. 89, no. 9, Sep. 2018, Art. no. 094705.

[15] K. Bayat, J. Choy, M. Farrokh Baroughi, S. Meesala, and M. Loncar, "Efficient, uniform, and large area microwave magnetic coupling to NV centers in diamond using double split-ring resonators," *Nano Lett.*, vol. 14, no. 3, pp. 1208–1213, Mar. 2014.

[16] N. Zhang *et al.*, "Microwave magnetic field coupling with nitrogen-vacancy center ensembles in diamond with high homogeneity," *Appl. Magn. Reson.*, vol. 47, no. 6, pp. 589–599, Jun. 2016.

[17] P. L. Stanwix *et al.*, "Coherence of nitrogen-vacancy electronic spin ensembles in diamond," *Phys. Rev. B, Condens. Matter*, vol. 82, no. 20, Nov. 2010, Art. no. 201201.

[18] A. Hajimiri, "The future of high frequency circuit design," in *Proc. ESSCIRC*, Sep. 2009, pp. 44–51.

[19] K. Sengupta and A. Hajimiri, "A 0.28 THz power-generation and beam-steering array in CMOS based on distributed active radiators," *IEEE J. Solid-State Circuits*, vol. 47, no. 12, pp. 3013–3031, Dec. 2012.

[20] Z. Hu, M. Kaynak, and R. Han, "High-power radiation at 1 THz in silicon: A fully scalable array using a multi-functional radiating mesh structure," *IEEE J. Solid-State Circuits*, vol. 53, no. 5, pp. 1313–1327, May 2018.

[21] ANSYS Inc. *High Frequency Structure Simulator (HFSS) User Guide, Version 18.1*. Accessed: Sep. 2018. [Online]. Available: http://www.ansys.com/

[22] L. Hong, H. Li, H. Yang, and K. Sengupta, "Fully integrated fluorescence biosensors on-chip employing multi-functional nanoplasmonic optical structures in CMOS," *IEEE J. Solid-State Circuits*, vol. 52, no. 9, pp. 2388–2406, Sep. 2017.

[23] A. D. Rakić, A. B. Djurišić, J. M. Elazar, and M. L. Majewski, "Optical properties of metallic films for vertical-cavity optoelectronic devices," *Appl. Opt.*, vol. 37, no. 22, p. 5271, 1998.

[24] H.-J. Hagemann, W. Gudat, and C. Kunz, "Optical constants from the far infrared to the X-ray region: Mg, Al, Cu, Ag, Au, Bi, C, and Al_2O_3," *J. Opt. Soc. Amer.*, vol. 65, no. 6, pp. 742–744, 1975.

[25] H. F. Talbot, "Facts relating to optical science. No. IV," *London, Edinburgh, Dublin Philos. Mag. J. Sci.*, vol. 9, no. 56, pp. 401–407, 1836.

[26] A. Wang and A. Molnar, "A light-field image sensor in 180 nm CMOS," *IEEE J. Solid-State Circuits*, vol. 47, no. 1, pp. 257–271, Jan. 2012.

[27] C. Wang, B. Perkins, Z. Wang, and R. Han, "Molecular detection for unconcentrated gas with ppm sensitivity using 220-to-320-GHz dual-frequency-comb spectrometer in CMOS," *IEEE Trans. Biomed. Circuits Syst.*, vol. 12, no. 3, pp. 709–721, Jun. 2018.

[28] C. Wang, X. Yi, J. Mawdsley, M. Kim, Z. Wang, and R. Han, "An on-chip fully electronic molecular clock based on sub-terahertz rotational spectroscopy," *Nature Electron.*, vol. 1, no. 7, pp. 421–427, Jul. 2018.

[29] V. M. Acosta, E. Bauch, M. P. Ledbetter, A. Waxman, L.-S. Bouchard, and D. Budker, "Temperature dependence of the nitrogen-vacancy magnetic resonance in diamond," *Phys. Rev. Lett.*, vol. 104, no. 7, pp. 1–4, Feb. 2010.

[30] T. Oeckinghaus, R. Stöhr, R. Kolesov, J. Tisler, F. Reinhard, and J. Wrachtrup, "A compact, diode laser based excitation system for microscopy of NV centers," *Rev. Sci. Instrum.*, vol. 85, no. 7, Jul. 2014, Art. no. 073101.

[31] D. Kasahara *et al.*, "Demonstration of blue and green GaN-based vertical-cavity surface-emitting lasers by current injection at room temperature," *Appl. Phys. Exp.*, vol. 4, no. 7, Jul. 2011, Art. no. 072103.

[32] J. F. Barry *et al.*, "Sensitivity optimization for NV-diamond magnetometry," 2019, *arXiv:1903.08176*. [Online]. Available: http://arxiv.org/abs/1903.08176

[33] F. Jelezko, T. Gaebel, I. Popa, A. Gruber, and J. Wrachtrup, "Observation of coherent oscillations in a single electron spin," *Phys. Rev. Lett.*, vol. 92, no. 7, Feb. 2004, Art. no. 076401.

[34] D. R. Glenn, D. B. Bucher, J. Lee, M. D. Lukin, H. Park, and R. L. Walsworth, "High-resolution magnetic resonance spectroscopy using a solid-state spin sensor," *Nature*, vol. 555, no. 7696, p. 351, 2018.
[35] J.-C. Jaskula, K. Saha, A. Ajoy, D. J. Twitchen, M. Markham, and P. Cappellaro, "Cross-sensor feedback stabilization of an emulated quantum spin gyroscope," *Phys. Rev. A, Gen. Phys.*, vol. 11, no. 5, May 2019, Art. no. 054010, doi: 10.1103/PhysRevApplied.11.054010.
[36] C. L. Degen, F. Reinhard, and P. Cappellaro, "Quantum sensing," *Rev. Mod. Phys.*, vol. 89, Jul. 2017, Art. no. 035002.

Mohamed I. Ibrahim (Student Member, IEEE) received the B.Sc. degree (Hons.) and the M.Sc. degree in electrical engineering from Ain Shams University, Cairo, Egypt, in 2012 and 2016, respectively. He is currently pursuing the Ph.D. degree with Electrical Engineering and Computer Science (EECS) Department, Massachusetts Institute of Technology (MIT), Cambridge, MA, USA.

From 2012 to 2016, he was a Teaching and Research Assistant with Ain Shams University. He was also developing metamaterial inspired antennas and microwave passive structures. Since he started his Ph.D. at MIT in 2016, he has been developing integrated systems for quantum computing and sensing applications using hybrid CMOS and spin-based semiconductor defects platforms. He is also working on low-power smart wireless tagging and monitoring systems. His research interests include microelectronic circuits for quantum systems, millimeter-wave and THz wireless systems, and novel electromagnetic materials and devices.

Christopher Foy received the B.Sc. degree from the Physics Department, Georgia Institute of Technology, Atlanta, GA, USA, in 2012, and the M.Sc. degree in electrical engineering from the Massachusetts Institute of Technology (MIT), Cambridge, MA, USA, in 2016, where he is currently pursuing the Ph.D. degree.

He is working on quantum sensing with the Spin-Based Defect Center located in diamond called the Nitrogen Vacancy center. He is interested in both improving the breadth and depth of this sensing platform for both magnetometry and thermometry. His research interests include quantum sensing, optics, advanced metrology, and materials and devices.

Dirk R. Englund (Member, IEEE) received the B.S. degree in physics from Caltech, Pasadena, CA, USA, in 2002, the M.S. degree in electrical engineering from TU Eindhoven, Eindhoven, Netherlands, and the Ph.D. degree in applied physics from Stanford University, Stanford, CA, in 2008.

He was a Post-Doctoral Fellow with Harvard University, Cambridge, MA, USA, until 2010, when he started his group as an Assistant Professor of electrical engineering and of applied physics with Columbia University, New York, NY, USA. In 2013, he joined the Faculty of the Department of Electrical Engineering and Computer Science, MIT, Cambridge. His research focuses on quantum technologies based on semiconductor and optical systems.

Dr. Englund was a recipient of the 2011 Presidential Early Career Award for Scientists and Engineers, the 2011 Sloan Research Fellowship in Physics, the 2012 DARPA Young Faculty Award, the 2012 IBM Faculty Award, an 2016 R&D100 Award, the OSA's 2017 Adolph Lomb Medal, and the 2017 ACS Photonics Young Investigator Award.

Ruonan Han (Senior Member, IEEE) received the B.Sc. degree in microelectronics from Fudan University, Shanghai, China, in 2007, the M.Sc. degree in electrical engineering from the University of Florida, Gainesville, FL, USA, in 2009, and the Ph.D. degree in electrical and computer engineering from Cornell University, Ithaca, NY, USA, in 2014.

He is currently an Associate Professor with the Department of Electrical Engineering and Computer Science, Massachusetts Institute of Technology, Cambridge, MA, USA. His current research interests include microelectronic circuits and systems operating at millimeter-wave and terahertz frequencies.

Dr. Han was a recipient of the Cornell ECE Director's Ph.D. Thesis Research Award, the Cornell ECE Innovation Award, and the two Best Student Paper Awards of the IEEE Radio frequency Integrated Circuits Symposium in 2012 and 2017. He was also a recipient of the IEEE Microwave Theory and Techniques Society (MTT-S) Graduate Fellowship Award and the IEEE Solid-State Circuits Society (SSC-S) Predoctoral Achievement Award. He served as an Associate Editor for the IEEE TRANSACTIONS ON VERY-LARGE-SCALE INTEGRATION SYSTEM in 2019, the IEEE TRANSACTIONS ON QUANTUM ENGINEERING in 2020, a Guest Associate Editor for the IEEE TRANSACTIONS ON MICROWAVE THEORY in 2019 and Techniques, and also serves on the Technical Program Committee (TPC) for the IEEE RFIC Symposium and the 2019 Steering Committee and TPC of the IEEE International Microwave Symposium. He is the IEEE MTT-S Distinguished Lecturer from 2020 to 2022. He is the winner of the Intel Outstanding Researcher Award in 2019 and the National Science Foundation (NSF) CAREER Award in 2017.